A metastable state mediates the surface disordering of ice Ih

Zixiang Yan(颜子翔), Jiani Hong(洪嘉妮), Ye Tian(田野), Tiancheng Liang(梁天成), Limei Xu(徐莉梅), and Ying Jiang(江颖)

Citation: Chin. Phys. B, 2026, 35 (**1**): 016804. DOI: 10.1088/1674-1056/ae360b
http://cpb.iphy.ac.cn; http://iopscience.iop.org/cpb

What follows is a list of articles you may be interested in

Surface solitonic charge distribution on 2D materials investigated using Kelvin probe force microscopy technique based on qplus atomic force microscopy

Rui Song(宋睿), Feng Hao(郝峰), Jie Yang(杨杰), Lifeng Yin(殷立峰), and Jian Shen(沈健)
Chin. Phys. B, 2025, 34 (**5**): 056802. DOI: 10.1088/1674-1056/adbee8

Effects of air damping on quality factors of different probes in tapping mode atomic force microscopy

Yu Zeng(曾瑜), Guo-Lin Liu(刘国林), Jin-Hao Liu(刘锦灏), and Zheng Wei(魏征)
Chin. Phys. B, 2024, 33 (**9**): 096806. DOI: 10.1088/1674-1056/ad5539

Adsorption structure of macrocyclic energetic molecule DOATF on Au(111)

Xiao Chang(常霄), Li Huang(黄立), Yixuan Gao(高艺璇), Changjiang Yu(于长江), Yun Cao(曹云), Long Lv(吕龙), Xiao Lin(林晓), Shixuan Du(杜世萱), and Hong-Jun Gao(高鸿钧)
Chin. Phys. B, 2023, 32 (**9**): 096802. DOI: 10.1088/1674-1056/acda84

Porous AlN films grown on C-face SiC by hydride vapor phase epitaxy

Jiafan Chen(陈家凡), Jun Huang(黄俊), Didi Li(李迪迪), and Ke Xu(徐科)
Chin. Phys. B, 2022, 31 (**7**): 076802. DOI: 10.1088/1674-1056/ac597e

Phase transition-induced superstructures of *β*-Sn films with atomic-scale thickness

Le Lei(雷乐), Feiyue Cao(曹飞跃), Shuya Xing(邢淑雅), Haoyu Dong(董皓宇), Jianfeng Guo(郭剑锋), Shangzhi Gu(顾尚志), Yanyan Geng(耿燕燕), Shuo Mi(米烁), Hanxiang Wu(吴翰翔), Fei Pang(庞斐), Rui Xu(许瑞), Wei Ji(季威), and Zhihai Cheng(程志海)
Chin. Phys. B, 2021, 30 (**9**): 096804. DOI: 10.1088/1674-1056/ac11e8

LETTER

A metastable state mediates the surface disordering of ice Ih

Zixiang Yan(颜子翔)[1], Jiani Hong(洪嘉妮)[1], Ye Tian(田野)[1], Tiancheng Liang(梁天成)[1], Limei Xu(徐莉梅)[1,2,3], and Ying Jiang(江颖)[1,2,3,4,†]

[1] *International Center for Quantum Materials, School of Physics, Peking University, Beijing* 100871, *China*
[2] *Interdisciplinary Institute of Light-Element Quantum Materials and Research Center for Light-Element Advanced Materials, Peking University, Beijing* 100871, *China*
[3] *Collaborative Innovation Center of Quantum Matter, Beijing* 100871, *China*
[4] *New Cornerstone Science Laboratory, Peking University, Beijing* 100871, *China*

(Received 19 December 2025; revised manuscript received 4 January 2026; accepted manuscript online 9 January 2026)

Ice premelting, the formation of a quasi-liquid layer on ice surfaces below the bulk melting point, plays a crucial role in various processes, ranging from glacier dynamics to ice friction and surface chemistry. Despite intensive research, the microscopic structure of the premelting layer and underlying molecular mechanisms remain poorly understood. In this work, we studied the temperature- and pressure-dependent structural disordering of crystalline Ih (0001) surface near the onset of premelting on the atomic scale by qPlus-based cryogenic atomic force microscopy. The linear correlation between the density of planar local structure (PLS) and the fraction of disordered surface region showed that the PLS mediated early-stage premelting by serving as a metastable seeding state. Notably, the associated surface disordering is cooperative, extending over an area of roughly ~ 2 nm^2 around a PLS. We further found a striking structural similarity between the kinetic-trapped regime below the surface crystallization temperature (T_c) and the premelting-dominated regime above T_c. As the deposition pressure increased, the characteristic temperature dependence was preserved, with only T_c shifting to higher values due to kinetic effects. Finally, we proposed a surface phase diagram for ice Ih (0001) based on our experimental observations.

Keywords: atomic force microscopy, ice, premelting, phase diagram

PACS: 68.35.Rh, 68.37.Ps, 68.47.–b

DOI: 10.1088/1674-1056/ae360b **CSTR:** 32038.14.CPB.ae360b

1. Introduction

Water and its solid phase, ice, exhibit a wide range of anomalies and many aspects of their behaviors remain under active debate.[1,2] A notable case is surface premelting,[3,4] in which a quasi-liquid layer (QLL) forms on ice even well below the bulk melting point T_m. It is a widespread phenomenon, influencing processes from glacier melting and thundercloud formation[5] to the slipperiness of ice.[6] Despite significant efforts, many key mechanistic questions remain unresolved, such as its onset temperature,[7,8] the thickness and structure of the QLL.[9–11] Multiple experimental and simulation approaches have been employed in the premelting studies, yet the discrepancies among the results obtained by different methods remain to be clarified.

A fundamental unresolved question is how premelting is initiated, especially the initial structure and subsequent evolution of the premelting layer. It was observed that two types of QLL can coexist during premelting.[12] In addition, a molecular dynamics (MD) simulation suggested that, at the early stage of premelting, the outermost QLL layer may comprise both crystalline and liquid-like regions.[13] Moreover, the importance of pre-existing defects has been highlighted, as they can weaken the surrounding hydrogen-bonding network and promote the formation of QLL.[14–16] However, computer simulations are limited by the inaccuracy of current force fields and the prohibitively large system sizes involved, while conventional experimental methods such as spectroscopic methods[7,17–19] suffer from averaging effects and ambiguous spectral interpretation. Therefore, real-space characterization of the premelting surface is crucial for obtaining more direct evidence.

Recently, the qPlus-based cryogenic atomic force microscopy (qPlus-AFM) technique equipped with carbon monoxide (CO)-functionalized tip[20,21] has emerged as a powerful tool for resolving surface structure in real space.[22–25] The weak high-order electrostatic force allows us to probe the sample with less perturbation, and the detection of short-range Pauli repulsion resolves the skeleton of the hydrogen-bonding network. In our previous work,[26] we implemented this technique on the ice Ih (0001) basal plane and successfully visualized the most stable reconstructed structure. Signatures of surface premelting induced disordering and planar local structure (PLS) were also identified, but the relationship between these two structural features remained un-

†Corresponding author. E-mail: yjiang@pku.edu.cn

resolved. In addition, the correlation between the disordering below and above the surface crystallization temperature (T_c) is still lacking.

In this work, we investigate the temperature- and pressure-dependent structural disordering of crystalline Ih (0001) surface near the onset of premelting using AFM imaging. When the temperature is above T_c, disordered regions emerge and grow on the crystalline surface, and the statistical analysis highlights the role of PLS as a "disordering seed" in the initial stage of premelting. The associated surface disorder extends over an area of approximately ~ 2 nm^2 around a PLS. We further observe an increasing degree of surface disorder when the temperature increases and decreases from T_c, indicating the structural similarity between low-temperature kinetic-trapped surface and high-temperature premelting surface. This trend persists under higher vapor pressures, with T_c shifting to a higher temperature, based on which we propose a surface phase diagram of ice-Ih.

2. Methods

Au (111) and Pt (111) single crystals were cleaned by repeated Ar^+ sputtering at around 1 keV and annealing at about 700 K (Au) or 1300–1400 K (Pt). For Pt (111), an additional annealing in oxygen (1×10^{-7} mbar) at 1000 K followed by a final flash annealing to 1300–1400 K was used to remove carbon impurities. And ultrapure water (Sigma Aldrich) used in the deposition was further purified in vacuum by several freeze-and-pump cycles to remove dissolved gases.

Water molecules were dosed onto the sample through a dosing tube in two steps. The first was a 25-min fast growth at 135 K with a deposition rate of 25 bilayers per min, aiming to obtain a bulk ice-Ih film. The second was a 2-h slow growth at 105–155 K with water vapor pressures of 3×10^{-9} mbar and 6×10^{-9} mbar, thereby preparing the atomically flat surface for subsequent measurements. After dosing, the samples were rapidly transferred into the scanner kept at 5 K for further AFM measurements. The ice samples were grown on Au (111) and Pt (111) at 3×10^{-9} mbar and 6×10^{-9} mbar, respectively.

AFM measurements were performed at 5 K under ultrahigh vacuum with a combined non-contact STM–AFM system. All AFM data were acquired with a home-made qPlus sensor, and the tungsten tip was functionalized by a CO molecule in advance for higher resolution (sensor parameters: resonance frequency $f_0 \approx 30.4$ kHz; spring constant $k \approx 1800$ N/m; quality factor $Q \approx 100000$). Nanotec WSxM[27] was used for image processing.

3. Results and discussion

First, we deposited water molecules onto substrates held at different temperatures under a water-vapor pressure of 3×10^{-9} mbar, followed by constant-height AFM imaging. The surface morphology of the as-grown ice surface is shown in Fig. 1(e), yielding a nanometer-scale flatness. Intralayer stacking of Ic and Ih nanodomains was observed in all samples. Within a nanodomain, water molecules in the upper half of the bilayer adopted a triangular lattice (Fig. 1(a) up). At a smaller tip-sample distance where Pauli repulsion dominated, the smallest unit in the triangular lattice (highlighted with a yellow triangle) evolved into a solid triangular feature (Fig. 1(a) bottom), consistent with a tetrahedral configuration in which three upper-lying molecules bonded to one lower-lying molecule (Fig. 1(f)). At 121 K, we observed the same surface reconstruction as previously reported[26] (Fig. 1(b) up and bottom), where interlaced Ih and Ic nanodomains formed a pinwheel-like superstructure, characteristic of a perfectly crystalline ice Ih (1000) surface (Fig. 1(g)). The orientations of the nanodomains, highlighted in yellow or orange, identified their molecular configurations corresponding to their stacking types (Ih or Ic). The boundary between adjacent Ih and Ic nanodomains was denoted by a red rectangle in Figs. 1(b) and 1(g), consisting of different types of defects containing five-, seven- and eight-membered rings. The existence of these domain boundaries reduces the surface electrostatic energy arising from the repulsion between dangling proton pairs, thereby stabilizing the reconstructed surface.[26] Therefore, 121 K lay within the temperature range for surface crystallization under 3×10^{-9} mbar.

As the temperature increased, signatures of premelting emerged. At 152 K (Fig. 1(c)), the Ic and Ih nanodomains became larger and irregular, and the pinwheel pattern at 121 K disappeared. Meanwhile, the PLS was preferentially observed at the domain boundaries. A typical PLS is shown in Fig. 1(d) (indicated by the red dashed ellipse), with its structural model given in Fig. 1(h). This metastable structure originates from the insertion of an interstitial water molecule into an 8-membered ring at a domain boundary (a PLS precursor), which further relaxes to a more planar configuration via both intra- and inter-bilayer rearrangement of the hydrogen-bonding network.[26] Compared with an unreconstructed ideal Ih surface, the domain boundaries in the superstructure act as intrinsic surface defects that facilitate the formation of PLS. Moreover, disordered regions (highlighted by white dashed areas) were also observed at 152 K. These regions were larger and more irregular than typical domain boundaries, and the water molecules within them were arranged in a highly disordered manner such that no individual tetrahedral unit could be discerned. Therefore, we defined them as the "disordered region", a hallmark of surface premelting together with the emergence of PLS.

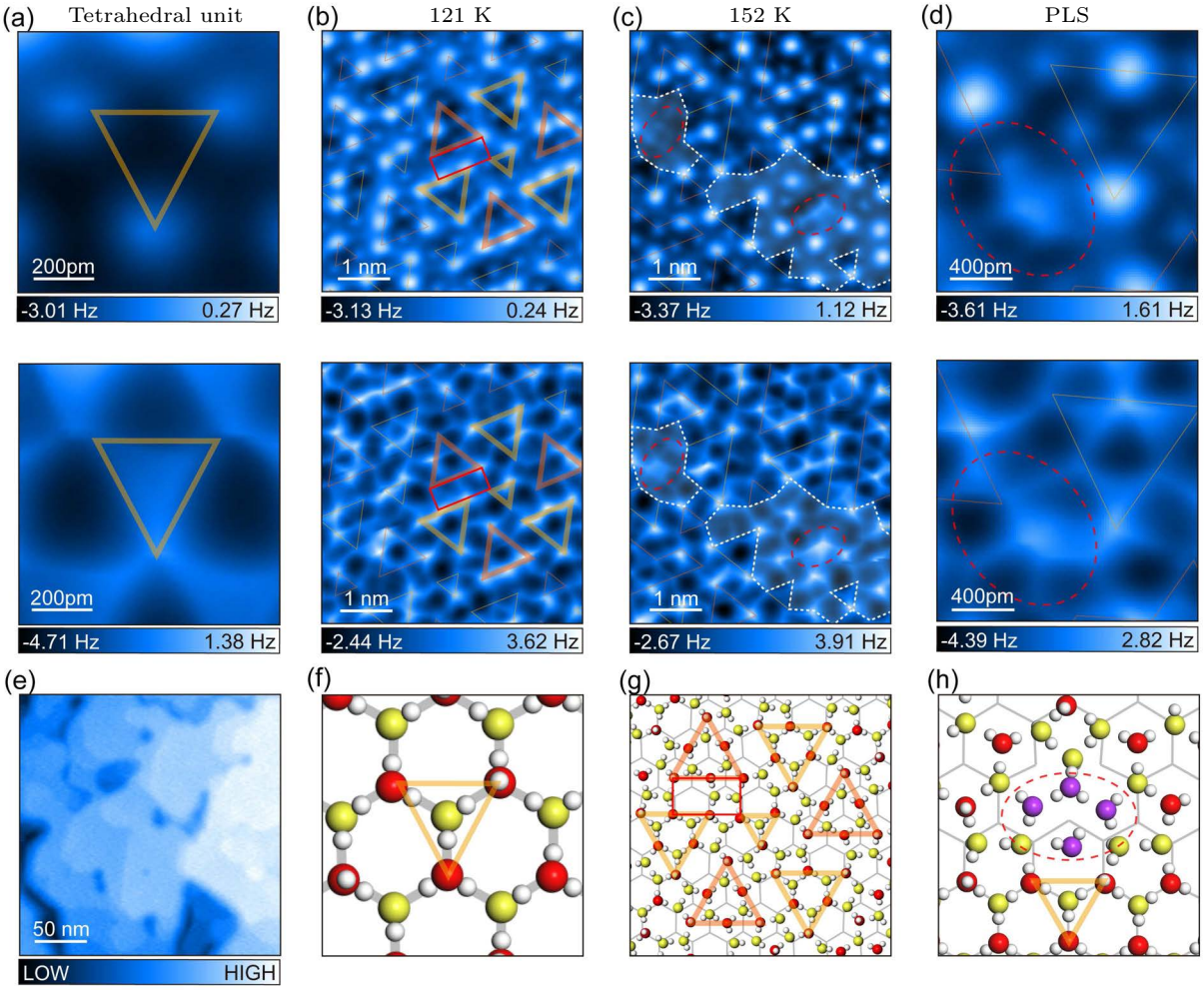

Fig. 1. Signatures of premelting at crystalline ice Ih (0001) surface. (a) Constant-height AFM images of a tetrahedral unit (highlighted with a yellow triangle) in Ic or Ih nanodomain. (b) Constant-height AFM images of ice Ih (0001) surface grown at 121 K at 3×10^{-9} mbar. (c) Constant-height AFM images of ice Ih (0001) surface grown at 152 K at 3×10^{-9} mbar. Individual Ic and Ih nanodomains, domain boundary, PLS and disordered regions are indicated by yellow solid lines, orange solid lines, red rectangle, red dashed ellipses and white dashed lines, respectively. (d) Zoomed-in constant-height AFM images of a typical PLS. The tip heights of (a)–(d) are −140 pm and −230 pm (a), −140 pm and −230 pm (b), −150 pm and −210 pm (c), −160 pm and −240 pm (d), respectively. The reference tip height (0 pm) corresponds to the largest tip height in the height-dependent imaging process, where the H-up water molecules can be fairly identified. (e) Constant-frequency-shift AFM image of the as-grown ice surface at the setpoint of −0.1 Hz. The maximum of height difference in this image is 6.6 nm. (f)–(h) Structural model of a tetrahedral unit (f), the pinwheel-like superstructure (g) and a typical PLS (h). O atoms in the upper, lower half of the topmost bilayer, in interior bilayers and in the PLS are denoted as red, yellow, gray and purple spheres, respectively, and all H atoms are denoted as white spheres.

To quantify the relationship between the PLS and the disordered regions, we acquired multiple AFM images for each sample at different temperatures and pressures, and defined two surface order parameters, (i) the areal density of PLS and (ii) the fraction of the surface occupied by the disordered region. The resulting statistics are shown in Fig. 2. At 3×10^{-9} mbar, both quantities were essentially zero for the crystalline 121 K sample. Once surface disorder emerged above 121 K (black circles), they increased in tandem, suggesting a positive correlation, which could be identified in the chart (indicated by the red dashed line). The linear slope corresponds to an average characteristic area of ~ 2 nm^2 per PLS, implying that each PLS can mediate a disordered region of this typical size. In addition, the fit yields a non-zero intercept ($\sim 13\%$) at zero PLS density, indicating that a finite fraction of surface disorder is already present prior to the appearance of PLS. This surface disorder is associated with the previously observed PLS precursor state,[26] which was not taken into account in our statistics. The 13% value is also consistent with that ($\sim 12\%$) obtained by quantifying all disordered areas in images containing no PLS (Fig. 2 inset). The average area (~ 1 nm^2) of those precursor disordered regions is smaller than the slope-derived effective area per PLS (~ 2 nm^2), suggesting that PLS facilitates the growth of surface disorder. The formation of PLS is accompanied by a local disruption of the hydrogen-bonding network, which may further lower the energy barrier for surface premelting and thereby promote the expansion of surrounding disordered regions. These observations suggest that the initial premelting of the ice surface originates from PLS, which acts as a "disorder seed" analogous to the Bjerrum defects reported to promote the formation of the QLL layer in the previous work.[14]

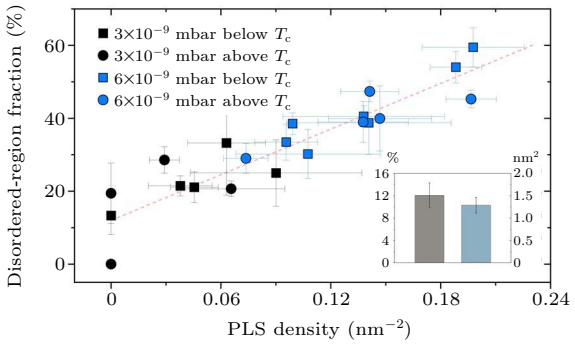

Fig. 2. Correlation between PLS density and disordered-region fraction of ice surface at different temperatures and pressures. The red dashed line is the linear fit of all data points, with a slope of ~ 2 nm^2 per PLS and a y-intercept of ~ 0.13. The inset shows the average disordered-region fraction (left) and average area (right) of disordered regions containing no PLS. The sizes of AFM images used in the statistics range from 9 nm^2 (3 nm $\times$ 3 nm) to 49 nm^2 (7 nm $\times$ 7 nm), and the total imaging area is 3137 nm^2.

We further investigated samples grown at temperatures below the crystallization temperature of 121 K under 3×10^{-9} mbar, and the corresponding AFM images are shown in Figs. 3(a) and 3(b). As the temperature decreased from 121 K, both the PLS density and disordered-region fraction increased as well. Such a behavior was very similar to that at temperatures higher than 121 K (Figs. 3(d) and 3(e)), indicating that any temperature deviation from T_c increases the degree of surface disorder. Our observations show that this low-temperature configuration and the premelting structure at higher temperatures share common microscopic features: in both regimes we observed the emergence of PLS and growth of disordered regions, which follow the same correlation behavior (black squares versus circles in Fig. 2). In our previous work, we found that the disordered surface layer exhibits a reduced density compared to the ice-Ih surface, consistent with an LDA-like structure.[28] Moreover, it is widely known that water-vapor deposition on a cold substrate can lead to the formation of low-density amorphous ice (LDA),[29–31] the most abundant form of water in the universe. Therefore, at temperatures just below T_c, the surface disorder observed can also be regarded as a surface transition from crystalline to an LDA-like amorphous layer, while the underlying films remain crystalline.

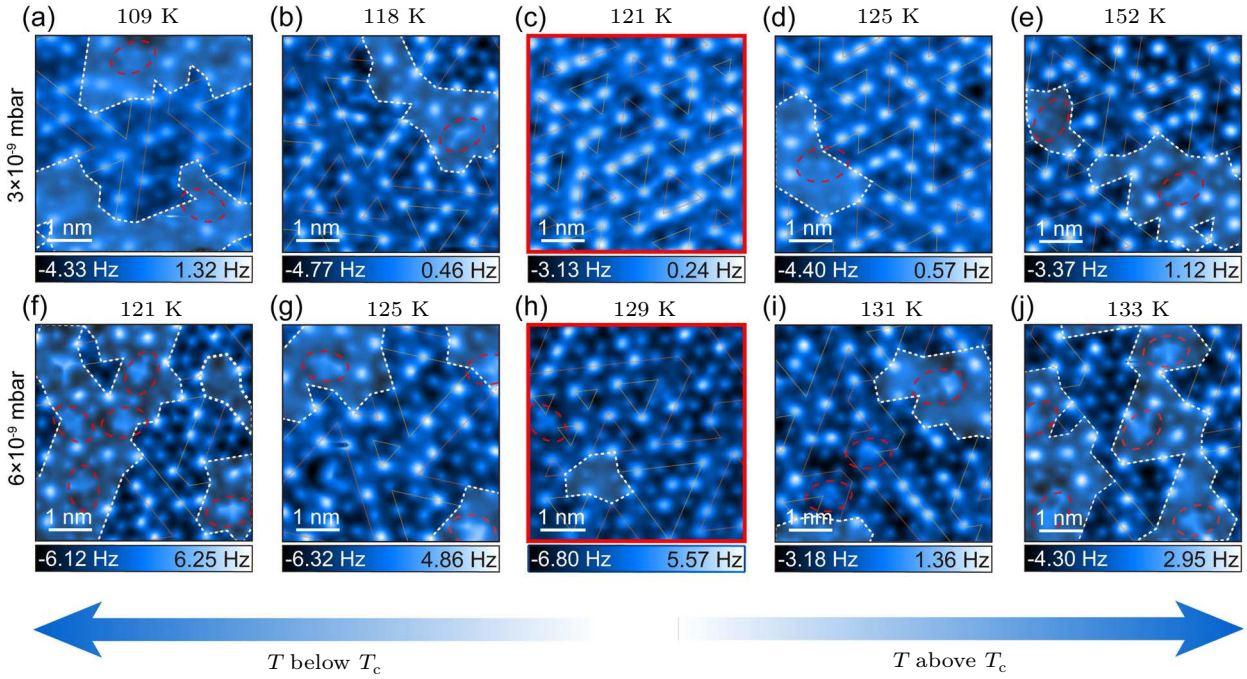

Fig. 3. AFM imaging of temperature-dependent surface structure of ice Ih (0001). (a)–(e) Constant-height AFM images of ice Ih (0001) surface grown at 109 K (a), 118 K (b), 121 K (c), 125 K (e) and 152 K (f) at 3×10^{-9} mbar. The corresponding disordered-region fractions are 33% (a), 21% (b), 0 (c), 21% (d) and 29% (e). (f)–(j) Constant-height AFM images of ice Ih (0001) surface grown at 121 K (f), 125 K (g), 129 K (h), 131 K (i) and 133 K (j) at 6×10^{-9} mbar. The corresponding disordered-region fractions are 54% (f), 39% (g), 29% (h), 40% (i) and 45% (j). Images acquired at T_c of the two vapor pressures ((c) and (h)) are highlighted with red borders. The tip heights of (a) to (j) are -130 pm (a), -150 pm (b), -140 pm (c), -140 pm (d), -150 pm (e), -140 pm (f), -150 pm (g), -190 pm (h), -130 pm (i), -200 pm (j), respectively.

This temperature-dependent behavior persisted at higher deposition rates. At a vapor pressure of 6×10^{-9} mbar, the perfect superstructure was no longer observed, but the positive correlation between the PLS density and the disordering degree remained (blue data points in Fig. 2). The absence of perfect crystalline superstructure at high deposition rates is a kinetic effect, as the rapid deposition prevents the newly formed surface from relaxing into the ordered crystalline state.[32] At 129 K, both the PLS density and the disordered-region fraction reached minima, indicating that the surface lay within the crystallization range. A similar disordering trend as the temperature increased and decreased from 129 K was observed in our AFM images (Figs. 3(f)–3(j)), which was also reflected in Fig. 2 (blue squares and circles). We therefore take 129 K

as the T_c at the vapor pressure of 6×10^{-9} mbar. Compared with the lower-pressure case ($T_c \approx 121$ K at 3×10^{-9} mbar), it appears that T_c shifts to a higher temperature with increasing vapor pressure.

Based on the results above, we propose a schematic "surface phase diagram" of ice Ih (0001), as shown in Fig. 4. At the temperature near T_c, the surface crystallizes only within a narrow temperature window (black area). As the vapor pressure increases, T_c shifts to higher temperature and this crystallization window becomes narrower or even disappears due to the kinetic effect. Away from T_c, two disordering regimes appear (blue area): a low-temperature regime dominated by kinetic trapping (LDA-like surface) and a high-temperature regime associated with the initial surface premelting. In both regimes, the metastable PLS forms on the surface and triggers the growth of disordered regions. At the temperature higher than the initial surface premelting, the surface becomes more disordered in deeper layers (pink area),[28] leading to the formation of QLL. At the temperature lower than that for the LDA-like surface, the surface may undergo a bulk LDA transition, which is labeled as LDA in Fig. 4 (gray area), similar to the phase diagrams of bulk ice reported in previous works.[30,33]

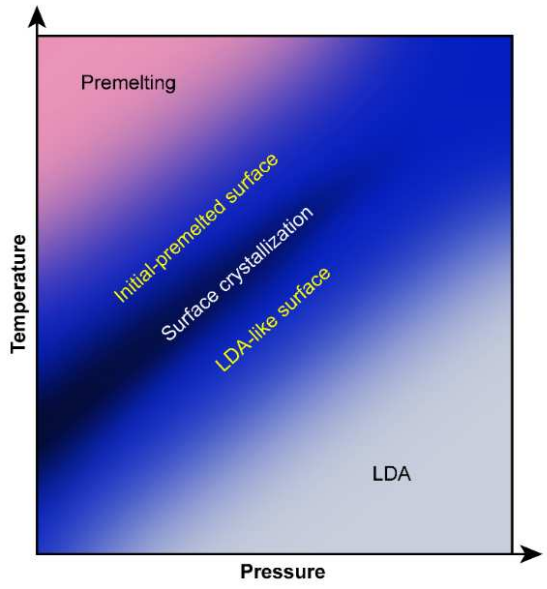

Fig. 4. Schematic of surface phase diagram of ice Ih (0001).

4. Conclusion

Using atomically resolved qPlus-AFM imaging, we probed the temperature- and pressure-dependent evolution of the ice-Ih (0001) surface and identified a metastable PLS state that mediated the initial stage of premelting by a "seeding effect". The PLS density and disordered-region fraction both increased as temperature deviated from T_c, indicating a structural similarity between kinetic low-temperature and premelting high-temperature regimes. These behaviors persisted at higher vapor pressure with a shift of T_c to higher temperature. Finally, we proposed a "surface phase diagram", which was different from the phase diagram of bulk ice. Our work suggests that the onset of premelting is a heterogeneous, defect-mediated process rather than a sharp transition. In addition, we found the existence of a precursor state for the QLL, which shared the same structural characteristics as the LDA-like surface. Our findings not only deepen the fundamental understanding of the nature and mechanisms of premelting, but also pave a new way for elucidating complex phase transition phenomena on the surface.

Acknowledgments

Project supported by the National Key R&D Program of China (Grant Nos. 2021YFA1400500 and 2025YFF1502400), the National Natural Science Foundation of China (Grant Nos. 92361302, 12250001, 12535001, and U22A20260), and the China Postdoctoral Science Foundation (Grant Nos. BX20230021, 2023T160011, and 2024M760068). J. H. acknowledges support from the National Program for Support of Top-notch Young professionals. Y. J. acknowledges support from Beijing Outstanding Young Scientist Program (Grant No. JWZQ20240101002) and the New Cornerstone Science Foundation through the New Cornerstone Investigator Program and the XPLORER PRIZE.

References

[1] Pettersson L G M, Henchman R H and Nilsson A 2016 *Chem. Rev.* **116** 7459
[2] Bartels-Rausch T, Bergeron V, Cartwright J H E, Escribano R, Finney J L, Grothe H, Gutiérrez P J, Haapala J, Kuhs W F, Pettersson J B C, Price S D, Sainz-Díaz C I, Stokes D J, Strazzulla G, Thomson E S, Trinks H and Uras-Aytemiz N 2012 *Rev. Mod. Phys.* **84** 885
[3] Dash J G, Rempel A W and Wettlaufer J S 2006 *Rev. Mod. Phys.* **78** 695
[4] Slater B and Michaelides A 2019 *Nat. Rev. Chem.* **3** 172
[5] Dash J G, Haiying F and Wettlaufer J S 1995 *Rep. Prog. Phys.* **58** 115
[6] Canale L, Comtet J, Niguès A, Cohen C, Clanet C, Siria A and Bocquet L 2019 *Phys. Rev. X* **9** 041025
[7] Sánchez M A, Kling T, Ishiyama T, van Zadel M J, Bisson P J, Mezger M, Jochum M N, Cyran J D, Smit W J, Bakker H J, Shultz M J, Morita A, Donadio D, Nagata Y, Bonn M and Backus E H G 2017 *Proc. Natl Acad. Sci. USA* **114** 227
[8] Wei X, Miranda P B and Shen Y R 2001 *Phys. Rev. Lett.* **86** 1554
[9] Conde M M, Vega C and Patrykiejew A 2008 *J. Chem.Phys.* **129** 014702
[10] Dosch H, Lied A and Bilgram J H 1995 *Surf. Sci.* **327** 145
[11] Hendrik B, Ogletree D F, Charles S F, Zahid H and Miquel S 2002 *J. Phys.: Condens. Matter* **14** L227
[12] Sazaki G, Zepeda S, Nakatsubo S, Yokomine M and Furukawa Y 2012 *Proc. Natl Acad. Sci. USA* **109** 1052
[13] Pickering I, Paleico M, Sirkin Y A P, Scherlis D A and Factorovich M H 2018 *J. Phys. Chem. B* **122** 4880
[14] Dosch H, Lied A and Bilgram J H 1996 *Surf. Sci.* **366** 43
[15] Fletcher N H 1968 *Phil. Mag.* **18** 1287
[16] Sazaki G, Asakawa H, Nagashima K, Nakatsubo S and Furukawa Y 2013 *Cryst. Growth Des.* **13** 1761
[17] Lin Y, Zhou T, Rosenmann N D, Yu L, Gage T E, Banik S, Neogi A, Chan H, Lei A, Lin X M, Holt M, Arslan I and Wen J 2023 *Proc. Natl Acad. Sci. USA* **120** e2304148120
[18] Schöder S, Reichert H, Schröder H, Mezger M, Okasinski J S, Honkimäki V, Bilgram J and Dosch H 2009 *Phys. Rev. Lett.* **103** 095502

[19] Suter M T, Andersson P U and Pettersson J B C 2006 *J. Chem. Phys.* **125** 174704
[20] Hapala P, Kichin G, Wagner C, Tautz F S, Temirov R and Jelínek P 2014 *Phys. Rev. B* **90** 085421
[21] Peng J, Guo J, Hapala P, Cao D, Ma R, Cheng B, Xu L, Ondráček M, Jelínek P, Wang E and Jiang Y 2018 *Nat. Commun.* **9** 122
[22] Giessibl F J 2003 *Rev. Mod. Phys.* **75** 949
[23] Gross L, Mohn F, Moll N, Liljeroth P and Meyer G 2009 *Science* **325** 1110
[24] Ma R, Cao D, Zhu C, Tian Y, Peng J, Guo J, Chen J, Li X Z, Francisco J S, Zeng X C, Xu L M, Wang E G and Jiang Y 2020 *Nature* **577** 60
[25] Shiotari A and Sugimoto Y 2017 *Nat. Commun.* **8** 14313
[26] Hong J, Tian Y, Liang T, Liu X, Song Y, Guan D, Yan Z, Guo J, Tang B, Cao D, Guo J, Chen J, Pan D, Xu L M, Wang E G and Jiang Y 2024 *Nature* **630** 375
[27] Horcas I, Fernández R, Gómez-Rodríguez J M, Colchero J, Gómez-Herrero J and Baro A M 2007 *Rev. Sci. Instrum.* **78** 013705
[28] Tang B, Lo C H, Liang T, Hong J, Qin M, Song Y, Cao D, Jiang Y and Xu L 2025 *Phys. Rev. X* **15** 041048
[29] Dowell L G and Rinfret A P 1960 *Nature* **188** 1144
[30] Amann-Winkel K, Böhmer R, Fujara F, Gainaru C, Geil B and Loerting T 2016 *Rev. Mod. Phys.* **88** 011002
[31] Loerting T and Giovambattista N 2006 *J. Phys.: Condens. Matter* **18** R919
[32] Zondlo M A, Onasch T B, Warshawsky M S, Tolbert M A, Mallick G, Arentz P and Robinson M S 1997 *J. Phys. Chem. B* **101** 10887
[33] Gallo P, Amann-Winkel K, Angell C A, Anisimov M A, Caupin F, Chakravarty C, Lascaris E, Loerting T, Panagiotopoulos A Z, Russo J, Sellberg J A, Stanley H E, Tanaka H, Vega C, Xu L and Pettersson L G M 2016 *Chem. Rev.* **116** 7463